nature communications

Article

https://doi.org/10.1038/s41467-025-59821-z

3D structure and dynamics of Campi Flegrei enhance multi-hazard assessment

Received: 10 September 2024

Accepted: 6 May 2025

Published online: 23 May 2025

Check for updates

G. De Landro[1], T. Vanorio[2], T. Muzellec[1,3], G. Russo[1], A. Lomax[4], J. Virieux[5] & A. Zollo[1]

Campi Flegrei is an active caldera in a populated area, currently experiencing significant ground uplift and seismicity. Leveraging seismicity relocations, here we obtain high resolution, 3D P- and S-wave seismic images which we combine with a tailored rock physics experiment to define key features of the caldera's structure: gas-rich reservoir below 2 km depth, deformed caprock at 1–2 km depth, and basement below 3.5 km depth. Seismicity migrates downwards from the caprock and changes in stress loading trigger deeper, higher events along the inner-caldera boundary faults. The reservoir closely correlates the area of maximum uplift, where deformation acceleration due to pore-fluid pressure is corroborated by laboratory experiments using site-relevant rock. The interaction between the pressurized gas-reservoir and the confining caprock drives the ground uplift. Our results indicate that seismic activity and the potential for a phreatic explosion should be considered as plausible scenarios, prompting a re-evaluation of the hazard assessment.

Over the past 50 years, the inner portion of the Campi Flegrei caldera (CFc) has experienced three major ground uplift episodes accompanied by intense seismic activity. The most recent episode began in 2005 and is still in progress[1] (Fig. 1). Ground deformation initially starts slowly but then accelerates[2], with the frequency and maximum magnitude of earthquakes also increasing with this acceleration[3] (Fig. 1B). The recent ground elevation rate is up to 2 cm per month. In the past year, several moderate, shallow earthquakes with magnitudes of M3.5+ (Fig. 1C) have caused strong ground shaking[4], raising concerns among the population and local authorities, and prompting calls for updated and reliable risk assessment.

CFc is a multi-hazard geological system where the primary natural hazards—ground instability, earthquakes, and volcanic eruptions—can interact in complex ways and potentially occur simultaneously or asynchronously, involving both mutual influence and independent triggering processes. Historical accounts preceding the last eruption of Monte Nuovo in 1538 describe a prolonged period of rapid ground uplift accompanied by intense seismic shaking, suggesting that elevated unrest often precedes volcanic activity[5]. These episodes of unrest during inter-eruption periods mark the onset of a volcanic crisis that may either culminate in an eruption or subside, ultimately returning to baseline levels of volcanic activity. Currently, volcanic hazard assessment involves identifying possible eruption scenarios based on a volcano's eruptive history and style, then linking these scenarios to hazards such as ballistic projectiles, lava flows, ashfall, pyroclastic density currents, and lahars[6]. At Campi Flegrei caldera probabilistic studies suggest that any new eruption would likely be moderate in scale, but still capable of producing ejection of large blocks near new vents, pyroclastic flows over several kilometers, and extensive ashfall that would likely affect Naples[7]. Phreato-magmatic explosions could further increase hazards in areas with hydrothermal activity or surface water[8]. In a co-production effort with scientists, disaster managers, and Civil Protection officials, an alert-level scheme has been established that uses monitored geophysical and geochemical parameters to determine when to escalate from low to high risk, initiating evacuation of the population[9].

A key question to advance our understanding of the CFc is: *What is the connection between the seismic signature of imaged structures and the temporal evolution of seismicity driven by deformation during periods of unrest?* Understanding this link offers a novel yet crucial

[1]Department of Physics 'Ettore Pancini', University of Naples 'Federico II', Naples, Italy. [2]Department of Earth and Planetary Sciences, Stanford Rock Physics and Geomaterials Laboratory, Stanford University, Stanford, CA, USA. [3]Department of Meteorology and Geophysics, University of Vienna, Vienna, Austria. [4]ALomax Scientific, Mouans-Sartoux, France. [5]ISTerre, Université Grenoble Alpes, CNRS, Grenoble, France. e-mail: aldo.zollo@unina.it

https://doi.org/10.1038/s41467-025-59821-z

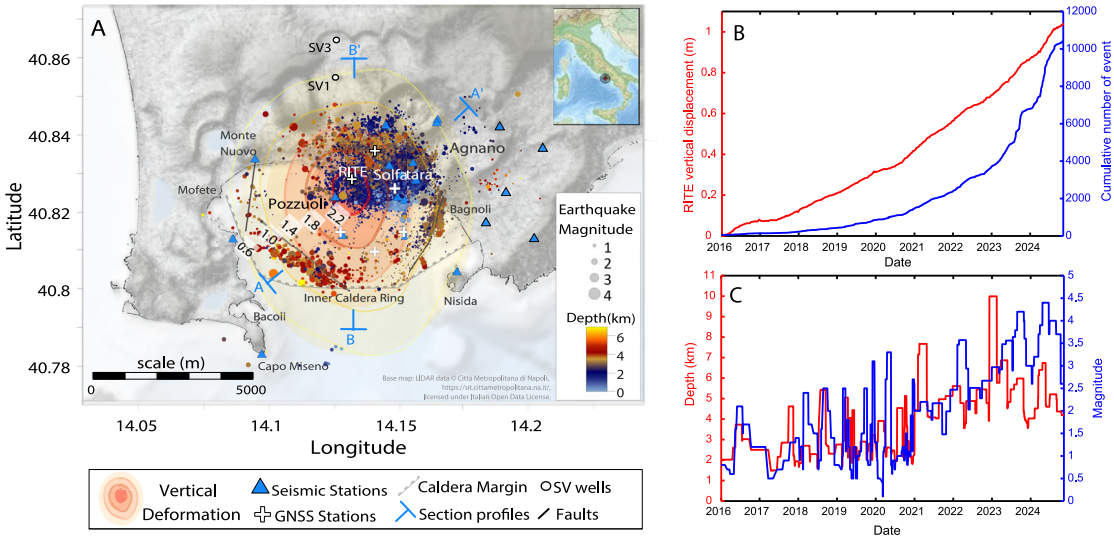

Fig. 1 | Visual representation of the unrest at the Campi Flegrei Caldera. **A** Epicentral distribution of seismic activity located in the final 3D model colored-coded as a function of depth together with the annular vertical displacement marked by red circles. Thickness and color-intensity denote the magnitude of uplift, the label indicates the vertical uplift in cm between January 2023 and June 2024. White triangles refer to seismic stations while white crosses indicate GNSS stations located within the first three uplift isolines. **B** Graph illustrating the temporal progression of uplift at the RITE station (red) alongside the evolution of the seismicity rate (blue) over the period 2000-2024. **C** Graph illustrating the temporal progression of maximum magnitude (red) and maximum depth (blue) of seismicity over the period 2000-2024. Source data of seismic catalog and ground deformation are provided as a Source Data file. Base map derived from Lidar data provided by the Città Metropolitana di Napoli (https://sit.cittametropolitana.na.it/), licensed under the Italian Open Data License (IODL).

perspective on underlying processes, enabling predictive capabilities and supporting informed decisions on resource allocation and protective measures for critical assets. Indeed, this knowledge not only informs hazard assessments but also shapes the urgency and timeline for implementing risk mitigation measures – particularly in densely populated cities near active volcanoes, where misjudgments could lead to significant loss of assets, economic disruption, and public distress.

As with other calderas, geophysical studies of CFc subsurface structures have yielded conflicting results[10], underscoring the need to correlate geophysical observations with rock physics properties[11] to better reconstruct the crust's structure and dynamics beneath the caldera.

Seismic imaging from active or passive data is a key method for reconstructing the 3D structure of the subsurface, both spatially and temporally[12,13]. Our current understanding of the CFc structure primarily comes from micro-seismicity data from the 1982–1984 unrest[14,15] and an extensive marine active seismic survey (SERAPIS[16], 2001). These studies provide an initial large-scale insight into velocity anomalies characterizing the inner caldera's physical properties while identifying the structures up to 8 km depth.

Using seismic reflection data from the SERAPIS survey, Zollo et al.[17] identified an extensive sill-like magmatic reservoir at about 8 km depth within the carbonate basement formation. Using linearized local earthquake tomography (LET) and analyzing thousands of earthquakes from the 1982–1984 crisis events, Vanorio et al.[18] found a low Vp/Vs ratio anomaly below 2 km depth. Since magmatic melt is incompatible with a low Vp/Vs ratio, this anomaly was interpreted through rock physics analysis as an over-pressured, gas-rich reservoir rather than a shallow magmatic reservoir. This interpretation is supported by subsequent seismic tomography studies[19,20] and seismic reflection data[17], which confirm the depth of this low Vp/Vs anomaly.

In contrast, later analyses utilizing the same seismic data from the 1982–1984 unrest[21,22] alongside gravimetric and deformation data[23] proposed a tentative association of geophysical anomalies with a melt zone at shallow depth (<5 km). Further expanding the dataset with 1500 additional micro-seismic events from 2005 to 2022, Giacomuzzi et al.[24] used a non-linear, Bayesian approach to generate 3D and 4D images of the inner caldera. The authors identified a km-size, low Vp and high Vp/Vs anomaly around 5 km depth in the caldera's center, which they interpret as a magma storage zone accumulating during the ongoing unrest.

By considering data from current unrest, around 5000 events from 2005 to 2023 and noise recordings, Calò and Tramelli[25] identified two high P-wave velocity and high Vp/Vs ratio bodies in the Pozzuoli caldera, both tied to fluid-rich structures at the resurgence block's edge. Despite the high Vp, the 3 km deep anomaly between Pozzuoli and Solfatara is interpreted as magmatic intrusion, conflicting with Giacomuzzi et al. (2024) finding of low Vp for the same anomaly. In addition, from modeling of geodetic observation, Astor et al.[26] tested the plausibility of different scenarios in investigating the source of current unrest mechanisms, suggesting that realistic scenarios should account for magma ascent to depths shallower than 8 km.

These conflicting results underscore the need for ongoing research to resolve discrepancies in the definition of subsurface structure, as they directly impact volcanic risk preparedness and mitigation strategies. The debate over melt migration at shallower depths arises due to the absence of seismicity between 5 and 8 km depth, which would indicate potential magma ascent along with its fluids[27,28].

In this study we integrate three main considerations to produce reliable tomographic images of the caldera's subsurface structure and properly interpret them. Firstly, regardless of the inversion approach employed, seismic imaging requires accurate a priori information in terms of velocity models and initial locations to produce interpretable final images. Hill[29] emphasized that rock property data from wells, including core samples, should guide the establishment of a geologically and physically reasonable a priori model. Secondly, seismic imaging from passive sources poses a multi-parametric challenge where source locations and velocity parameters are unknown, and thus jointly inverted. Additionally, imaging low-velocity zones from sources situated above the anomaly is difficult since seismic ray paths tend to avoid low velocity volumes. These issues can lead to trade-offs and increased uncertainty in subsurface imaging, unless

https://doi.org/10.1038/s41467-025-59821-z

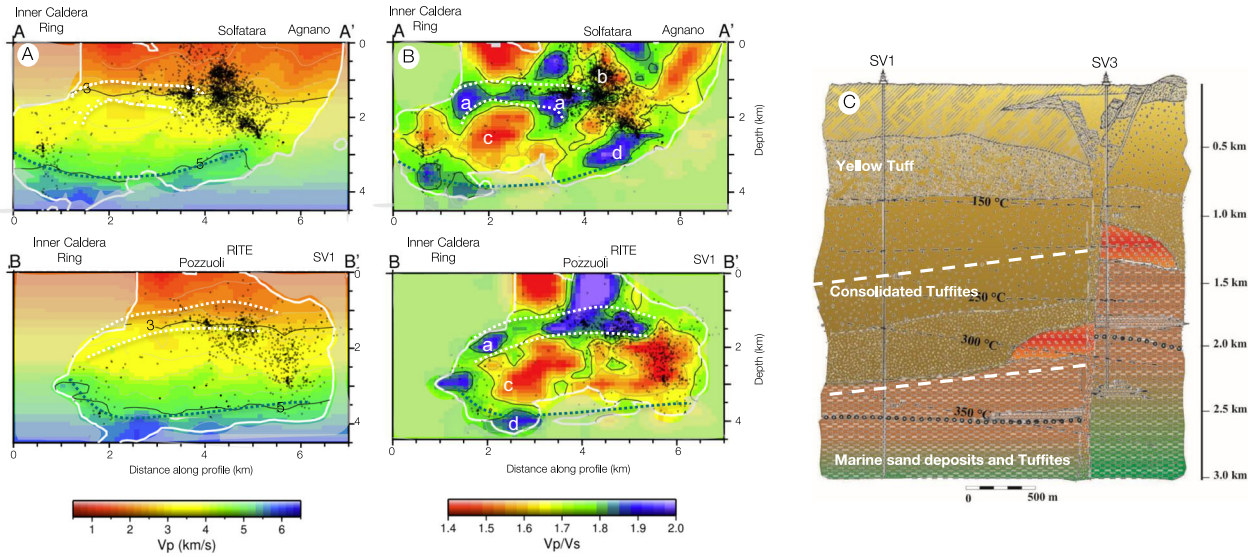

Fig. 2 | Tomographic models. Tomographic section Vp (**A**) and Vp/Vs (**B**) along AA′ and BB′ in Fig.1. Vp/Vs sections show several features: "a" layer with high Vp/Vs ratio (delineated with white dashed curves), associated to the caprock formation; "b" low Vp/Vs anomaly beneath the Solfatara; "c" low Vp/Vs well-confined volume, interpreted as a gas reservoir; "d" high Vp/Vs ratio, corresponding to a Vp higher than 5 km/s, compatible with a basement tilted toward SW (delineated with the dark green dashed line, correspondent to the Vp 5 km/s iso-velocity curve). The gas-bearing reservoir is within the siltite-tuffite formation[37] being confined between the caprock[34] (delineated by the white dashed lines) and the thermo-metamorphic limestone basement[49] (delineated with the dark green dashed line, corresponding to Vp 5 km/s iso-line). Black lines or contours indicate iso-velocity curves. The white contours enclose the resolved region. The resolution of S-phase models was used to define the Vp/Vs resolution. **C** Geological Section modified after Carella, R. and Guglielminetti[37] reconstructed from wells SV3 and SV1. Source data of Vp and Vp/Vs velocity models are provided as a Source Data file.

independently determined, high-quality source locations are utilized as constraints to mitigate errors from velocity model inaccuracies. Finally, the resolution of tomographic models, in both the covered volume and the smallest achievable grid size, depends on the spatial distribution and density of ray paths between data sources and network stations.

By utilizing a dataset of approximately 10,500 events acquired by the INGV (National Institute of Geophysics and Volcanology) permanent monitoring networks, located with an innovative location strategy (NLL-SSST[30]), we achieved unprecedented resolution in reconstructing the fine-scale structure of the CFc, down to a 250 m grid size by exploiting a multi-disciplinary strategy, from seismology to rock physics, to enhance imaging and interpretation accuracy.

The adopted probabilistic earthquake location method iteratively generates multi-scale, 3D source-specific station travel-time corrections, thereby minimizing the impact of velocity model error[3,30]. Our 3D iterative-perturbative Local Earthquake Tomography (LET) inversion strategy[31] employed a multi-scale inversion approach[32,33], conceptualizing the medium as a superposition of progressively smaller wavelength-scale grids, and initial P- and S-velocity models[18] based on rock properties from thirteen wells drilled in the CFc[34,35], which enables detailed imaging of subsurface structures. We demonstrated the robustness of the final tomographic images by using varying initial velocity models, all derived from the models based on rock properties (see Methods section for details). Finally, we based our interpretation of velocity anomalies on pore-pressure behavior from a rock physics experiments conducted with site-relevant core samples under caldera conditions.

In this work, this comprehensive, multi-parametric approach allowed us to identify three primary structures within the CFc and correlate them with the spatial, temporal, and magnitude distribution of microseismicity. Our findings clearly define the extent, geometry, and thickness of the gas-enriched (steam and CO_2) reservoir below 2 km, situated between an arc-shaped caprock and a basement structure. Initial low-magnitude seismicity occurs along the caprock before migrating downwards into the reservoir, facilitating fluid release. As the confined reservoir depressurized, the changing loading conditions on the caldera's border faults trigger deeper seismicity on pre-existing faults. Our results reveal a strong correlation between the reservoir's extent, ground uplift and seismicity, and the acceleration of pore fluid pressure deformation patterns observed in rock physics experiments. These findings suggest that the time-changing pressure field of the gas-enriched reservoir acting on the overlying fibrous microstructure of the caprock is the key element driving the Earth's surface ground deformation and, consequently, triggering the occurrence of seismicity, mostly along pre-existing inner caldera bordering faults[3].

Results

3D P- and S-wave Tomographic Images

The distribution of high-precision relocated seismicity is shown in Figs. 1A and 2A, B (see also Figs. S1, S2 in the Supplementary Material, SM). As for the seismicity accompanying the 1982–1984 unrest[15], the events are distributed along an ellipsoidal pattern following the inner Caldera ring. Most seismic activity occurs inland, beneath Pozzuoli and the Solfatara crater, at depths between 1 km and 4 km (Fig. 2A, B). A clear horizontal alignment of events is visible at 1–2 km depth onshore (see Fig. S1b, c in the SM). Deeper events are located offshore along the inner caldera ring[36] (Fig. 2A), where fault structures are evident as alignments of events in both plan views (gray lines in Fig. 1A) and section views (dashed black lines in Fig. S1b, c). Over time, the maximum magnitude and depth of seismicity increase along with increasing uplift (Fig. 1C).

Tomographic images of the CFc's structure are shown in Fig. 2 (for details on the inversion strategy, refer to the "Methods" section and Figs. S3–S6 in SM), displaying Vp (Fig. 2A) and the Vp/Vs ratio (Fig. 2B) along two vertical sections crossing the caldera (dashed lines AA′ and BB′ in Fig. 1A; horizontal slices of Vp and Vp/Vs models can be found in Figs. S7 and S8). The resolution analysis (see Method section for further details) allows us to assess that the models are resolved up down to 3.5–4 km depth (see Figs. S9, S10 in the SM), and

https://doi.org/10.1038/s41467-025-59821-z

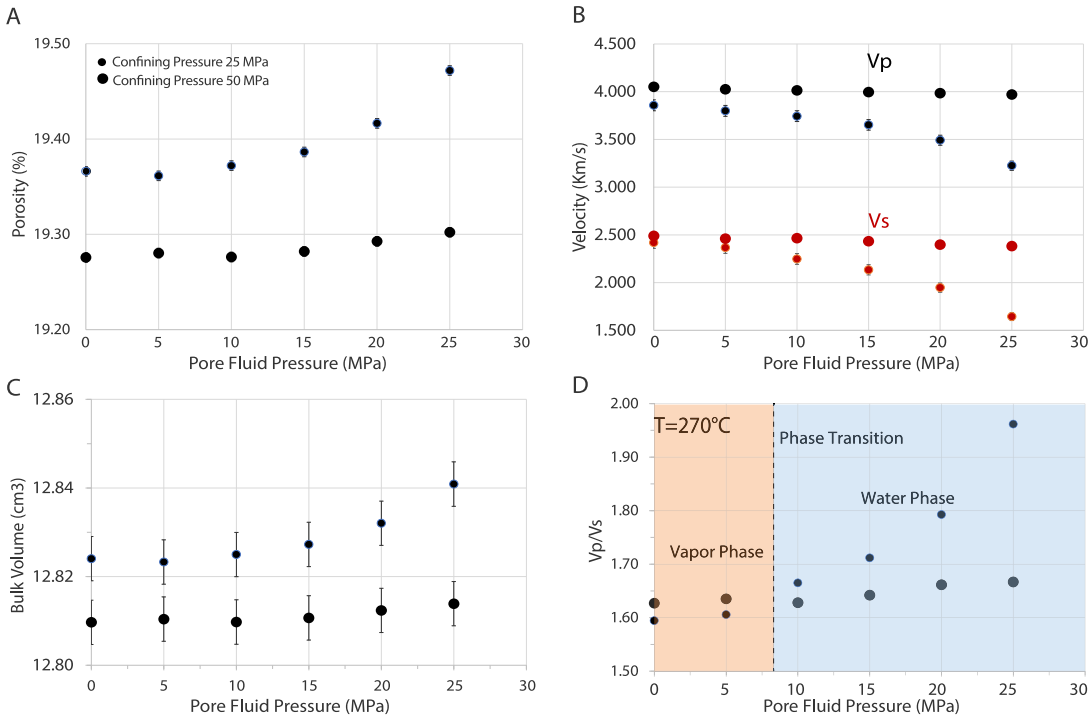

Fig. 3 | Rock physics experiment. Rock physics properties of a core plug from the rock formation at a depth of 2.5 km (Well SV1) in relation to pore fluid pressure. In the undrained experiment, water is injected into the sample while maintaining constant temperature and confining pressure to simulate conditions at a fixed depth of ~2.5 km. We measure the variations in porosity (**A**), P- and S-wave velocities (**B**), bulk volume (**C**), and the Vp/Vs ratio (**D**) in response to increasing pore pressure. As pore fluid pressure increases, there are simultaneous changes in both the properties of the rock frame and the fluid. With the injection of water into the sample, pore fluid pressure increases, leading to exponential expansion in both porosity (**A**) and bulk volume (**C**) of the sample. This increase causes a decrease in both P-wave and S-wave velocity, Vp and Vs, respectively (**B**). However, Vs experiences a more pronounced decline compared to Vp. This distinct behavior stems from the concurrent changes in the properties of the fluid being confined within the pore space. As pore fluid pressure rises under constant temperature, the fluid undergoes a transition from steam to liquid water (the vertical dashed line refers to the steam-liquid boundary on the water state PT diagram at the experimental temperature), resulting in enhanced stiffness (bulk modulus) of the fluid due to water's higher incompressibility compared to gas. This transition influences Vp but not Vs, thus enabling the change in fluid stiffness to counteract the increase in porosity, thus primarily affecting Vp. Consequently, the Vp/Vs ratio increases (**D**), being typical of a transition from gas-dominated to liquid-dominated pressurized formations. Source data of rock physics experiments are provided as a Source Data file.

minimum Vp/Vs ratios resolved variation is 0.13 (see Figs. S11, S12 in SM).

Three dominant features of the caldera's structure are clearly identified. Between 1 and 2 km depth, we detect a folded layer with Vp values of 3 to 4.5 km/s and a high Vp/Vs ratio (≥1.8, marked as "a" in Fig. 2B; Fig S8 in SM). This arc-like layer, approximately 800 m thick, extends through the middle of the caldera and corresponds to the tuffite formation depth shown in the geological section from SV1 and SV3 wells[37] (Fig. 2C; well locations in Fig. 1A). Beneath the Solfatara crater, this layer shows an interruption with a lower Vp/Vs ratio (≤1.6, marked as "b" in Fig. 2B; see Fig. S8 at 1.5 km depth in SM). Below this arc-shaped horizon, from 2 to 3.5 km depth, we identify a confined, near-ellipsoidal volume with a low Vp/Vs ratio ($1.4 \le Vp/Vs \le 1.55$, marked as "c" in Fig. 2B; see Fig. S8 at 2.5 km depth in SM) and a resolution greater than 0.9 (see Fig. S11 in SM). This feature is coherent with previous tomographic results, using data from both the 1982–84[18,22] and the ongoing crisis[24,25] that have already identified a low Vp/Vs layer below 2–3 km depth. However, the current study further delineates its shape and lateral extent. Finally, at depths of 3–4.5 km, we delineate a structure with P-wave velocities exceeding 5 km/s and a Vp/Vs ratio of about 1.75 (marked as "d" in Fig. 2B, see Fig. S7 in SM). This structure dips toward the caldera's center and presents, below the "c" volume, an elastic discontinuity characterized by Vp/Vs ratios ranging between 1.6 and 1.7. However, this feature is at the resolution limit and must be interpreted with caution.

Rock physics experiment

To interpret the tomographic velocity and Vp/Vs anomalies based on rock properties, we conducted laboratory experiments on site-relevant rock samples from the San Vito wells (SV1: 2125-2134 m and SV3: 1946-1950 m), which consist of a volcaniclastic siltite (see a scanning electron microscope image in Fig. S13). It consists of a quartz-dominated, marine siltite mixed volcanic material being referred to in the literature as tuffites[34,35,37]. These experiments are conducted under hydrothermal conditions, simulating temperature and pressure relevant to the caldera's depth within the reservoir below the caprock[34] (for further details, see "Methods"). Figure 3 shows how porosity, strain expressed as changes in bulk volume, P- and S-wave velocities, and Vp/Vs ratio vary with pore fluid pressure. Data were collected for two confining pressures to simulate lithostatic pressures compatible with depths of 1700 m and 2100 m. As water is progressively injected into the rocks, sustaining constant confining pressure and a temperature of 270 °C, pore fluid pressure increases. As a result, the effective stress decreases, leading to several observations. First, both porosity and bulk volume increase as the rock inflates due to rising pore pressure (Fig. 3A, B). This inflation is exponential with increasing pore pressure and is more pronounced at lower confining pressures. Second, Vp and Vs decrease as pore fluid pressure rises (Fig. 3C), with the decrease in Vs being more pronounced due to its independence from the elastic property of fluids. While Vp depends on the stiffness of the fluid, S-wave velocity does not depend on the fluid bulk modulus.

Consequently, Vs is not sensitive to the change in fluid phase (from vapor to liquid water, and vice versa) occurring as pore pressure changes. Conversely, the decrease in Vp, which results from the increased porosity and decreased stiffness at the grain contact of the rock frame, is counterbalanced by the increased stiffness of fluid as steam transitions to liquid water. The distinct behavior of the P- and S-wave velocities controls the increase in Vp/Vs as steam transforms into liquid water, with the changes being more pronounced at lower confining pressures (Fig. 3D). The steam-liquid transition is influenced by confining and pore fluid pressures. Confining pressure compresses pore spaces, which increases fluid flow resistance (i.e., decreases permeability), thus raising the pore fluid pressure required for the transition. Similarly, we expect that the stiffness of the rock frame (soft vs. stiff lithologies) also impacts the phase transition—by controlling strain under confining (burial) pressure, rock stiffness affects the available pore volume and hence, its ability to accumulate fluids.

Discussion

CFc structures and seismicity evolution

Over the past two years, the inner region of the CFc has experienced significant ground uplift acceleration, accompanied by increasing earthquake rates and magnitudes. During this period, deformation has also been marked by an incipient subsidence episode though mild and transient (e.g., summer 2024 from July to September). Using a large dataset of 10.500 seismic events, we defined three key elements of the CFc structure with greater spatial resolution, integrating the spatial characterization of structures at depth with the temporal distribution of seismicity. Not only does this analysis provide deeper insights into its subsurface framework, overall organization, and the dynamic functioning of its parts over time, but also lays the foundation for understanding the mechanisms driving the unrest. This includes assessing the associated ground deformation earthquake, and volcanic risks. By integrating tomographic images, site-specific rock properties from hydrothermal physics experiments, and high-precision spatial-temporal seismic events, we thus present a constrained, physics-based model of the CFc structure and its seismicity evolution with unprecedented spatial resolution (Fig. 4). The three primary structures within the CFc, along with the spatial and temporal evolution of its seismicity, are described below from the surface to depth:

(1) A Caprock Seal. At a depth of 1 to 2 km, a horizon with a relatively high Vp/Vs ratio (≥1.85, marked as "a" in Fig. 2B) exhibits an arc-like geometry. Its lateral extension is depicted in blue shades in Fig. 4B, highlighting the higher Vp/Vs region across the inner caldera. The spatial and temporal distribution of seismicity reveals that low-magnitude earthquakes recorded during the initial stage of the unrest are primarily concentrated within this bent layer (Fig. 4C, yellow-red shades). This layer corresponds to the caprock seal of about 1 km from wells separating the reservoirs both in San Vito and Mofete, and characterized by Vanorio et al.[11,18]. That is confirmed in subsequent tomographic studies[22,24,25]. Vanorio and Kanitpacharoen[11] characterized well cores from this horizon as being inherently fiber-reinforced due to pozzolanic cementation reactions occurring naturally within the caldera. Moreover, Vanorio et al.[38] provided evidence that hydrothermal water-vapor coexistence facilitates the sealing of caprock through the formation of the fibrous microstructure. It is well-established in the engineering community that fibers bridge cracks preventing brittle failure, and their entanglement[39,40] influence the mechanical response of materials favoring creeping and hence, a ductile failure behavior that increases toughness. Furthermore, specific P-T hydrothermal conditions promote growth and formation of mineral fibers[41]. Our study constrains the 3D lateral extent and thickness (~1 km) of this seal horizon, establishing a critical correlation with low-magnitude seismicity. This relationship underscores the creeping behavior of fiber-reinforced materials, providing key insights into the mechanical properties of this horizon and its seismogenic response. Specifically, the fibrous microstructure enables[11] the caprock to elastically deform into an arc-like shape, accommodating significant strain (up to 60 cm from 2011 to 2019, Fig. 1B). When deformation surpasses the rock seal's strength (45–74 MPa[11]), the caprock eventually reaches failure, triggering microseismicity while creeping. From an elastic standpoint, the caprock exhibits lateral heterogeneity. Notably, a region of caprock beneath the Solfatara crater shows lower Vp/Vs values (≤1.6, marked as "c" in Fig. 2B; yellow-green shades in Fig. 4B). Both modeling[18] and experiments (Fig. 3, this study) show that a decrease in Vp/Vs ratio indicates enrichment in steam saturation of the rock pore space. This condition corresponds to fractured or higher porosity rocks filled with vapor, which flow upward before condensing at lower depth temperature. This is supported by two observations reported in the literature: (1) the relatively high-resistivity plume beneath the Solfatara transitioning to low-resistivity at shallower depth (first 500–800 m)[42], and interpreted as a plume rising toward a highly active liquid-dominated reservoir; and (2) the relatively higher Vp/Vs[11,18,22] (>1.85) above the caprock within the first kilometer better resolved in the preset study (Fig. 2B, bottom panel), being indicative of predominant liquid water.

(2) A Gas-enriched Reservoir. Beneath the caprock, this study traces the extent, geometry, and thickness of a low Vp/Vs anomalous geobody (1.4 ≥ Vp/Vs ≤1.55, marked as "c" in Fig. 2B and shown in yellow-orange shades in Fig. 4), located between 2 and 4 km depth within the siltite-tuffite formation[34] (Fig. 2B) in the central area of CFc beneath Pozzuoli. Laboratory experiments on site-relevant samples[34,37] under hydrothermal conditions demonstrate that the observed low Vp/Vs values, between 1.5 and 1.6 (Fig. 3D), are compatible with a gas enriched reservoir (steam and CO_2), leading to overpressure conditions[18]. Leveraging these results, we show that strain in a porous medium, as indicated by increases in porosity and bulk volume (Fig. 3A–C), initially increases slowly then exponentially with rising pore fluid pressure. Such increases in reservoir porosity are known to significantly compromise its physical and mechanical properties.

The close spatial correlation between the gas-enriched reservoir and the caprock centered beneath the area of maximum uplift[2] at Pozzuoli (see Fig. 4A, B) forms the basis for understanding unrest mechanisms in the CFc, including the deformation and the temporal evolution of seismicity. Specifically, offshore larger-magnitude seismic events (Md > 3) occur at greatest depths, between 3 and 4 km (Fig. 1C–G), aligning with inner ring faults[36] at the southwestern reservoir border near Baia-Bacoli, and occurring later in time[3]. Following this deepest seismicity, higher-magnitude earthquakes (up to Md 4.2) closer to the shore near Bagnoli occur at depth below 2 km (see gold dots in Fig. 1A), delineating a ~N–S trending sub-vertical fault structure just offshore La Pietra[3]. This fault structure has activated later in time (Fig. 4E), during the current unrest at the reservoir's eastern border, producing larger-magnitude events up to 4.2. This evolution of seismicity is likely driven by dynamically changing loading conditions[43] on pre-existing faults bordering the caldera. Following the shallower seismicity in the central part of the caldera along the caprock (Fig. 4C, D), degassing through this seal horizon induces reservoir depressurization and depletion triggering seismicity at later stages (Fig. 4E–G). During such uplift episodes, as observed in Yellowstone[44] and above the Socorro Magma Body[45] (Mexico), pre-existing faults in highly fractured media experience reduced effective stress, while surrounding areas undergo changes in pore pressure and transient stress conditions. These combined

https://doi.org/10.1038/s41467-025-59821-z

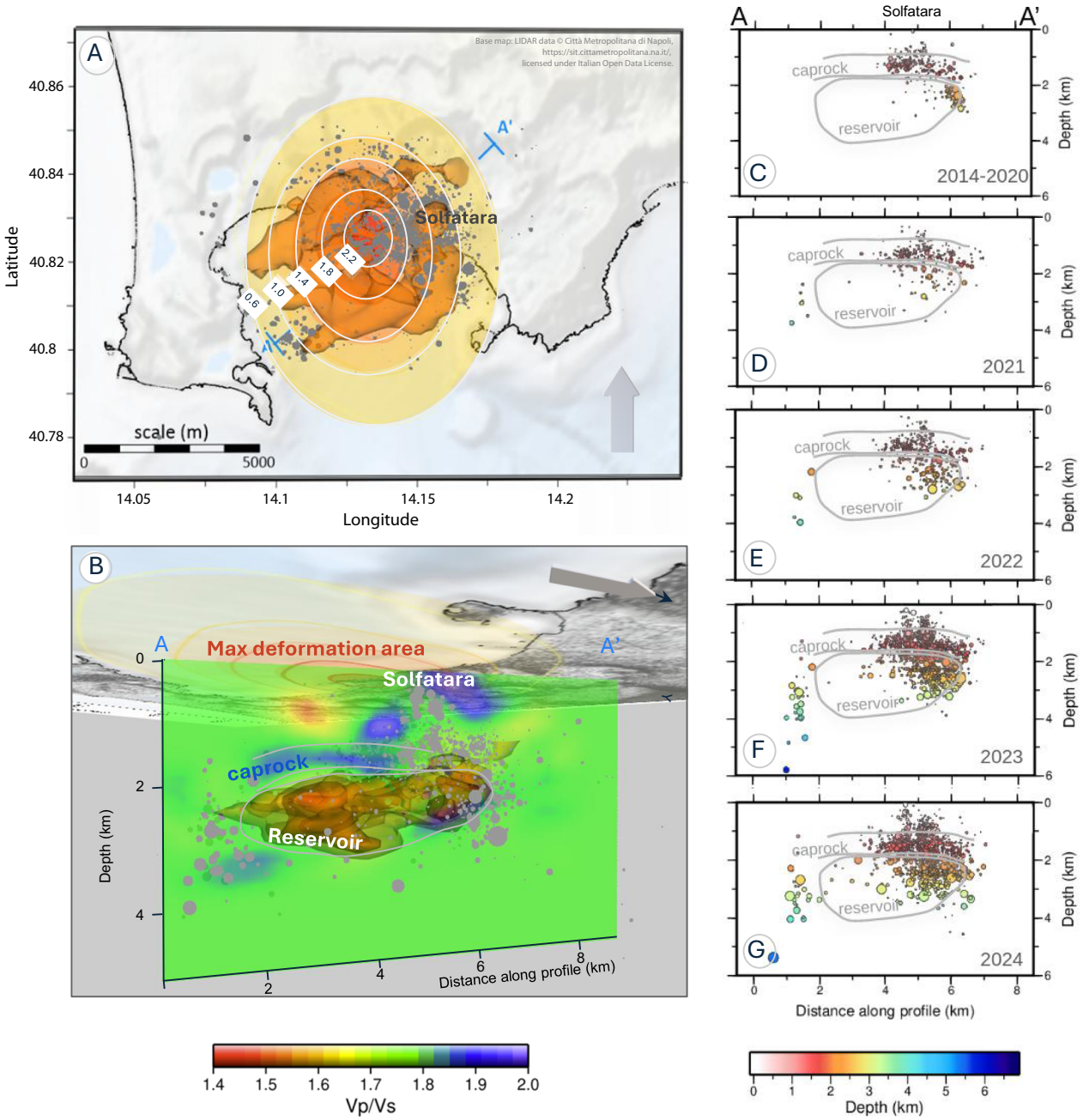

Fig. 4 | 3D Visualization of Vp/Vs anomalies within the Campi Flegrei Caldera. **A** Map view of the caldera illustrating deformation isolines, low Vp/Vs anomaly (orange body) and the orientations of the Vp/Vs profile of **B**, **C** panels. The arrow indicates the North direction. Thickness and color-intensity denote the magnitude of uplift, the label indicates the vertical uplift in cm between January 2023 and June 2024. **B** A schematic view of the Vp/Vs section along the AA' profile crossed by the isosurface of low Vp/Vs anomaly, interpreted as a gas reservoir. The arrow indicates the North direction. The reservoir is confined above by the caprock, identified by the high Vp/Vs anomaly. The region beneath the Solfatara represents an elastic discontinuity in the caprocks, evidenced by Vp/Vs values (depicted in yellow-green color shades) higher compared to those characterizing the gas reservoir and lower than those characterizing the caprock. This zone likely denotes an area of structural damage where fluids escape from the system. **C**–**G** Temporal evolution of seismic event locations from 2014 to 2024. Seismic events are color-coded according to depth, with circle size indicative of event magnitude. The spatial and temporal distribution of seismicity reveals that low-magnitude earthquakes occurring earlier are primarily located in the caprock, while larger-magnitude events occurring later in time align with faults bordering the caldera. Source data of seismic catalog and velocity models are provided as a Source Data file. Base map derived from Lidar data provided by the Città Metropolitana di Napoli (https://sit.cittametropolitana.na.it/), licensed under the Italian Open Data License (IODL).

mechanisms significantly amplify shallower, and much later, swarm seismicity along the region's pre-existing faults and fractures, such as those at Solfatara[46]. The temporal evolution of events directly reflects how the progressive depressurization of the reservoir leads to gradual reservoir depletion, thereby influencing loading on the caldera's bordering faults[38].

(3) Basement. Beneath the gas-enriched reservoir, we detected a basement structure (Fig. 2A) that dips toward the caldera's center. Previous studies have identified this concave shape through gravimetry[47] and seismic reflection[48]. This structure has a P-wave velocity of 5 km/s and a Vp/Vs ratio of about 1.75, reflecting reduced P-velocity and Vp/Vs associated with

thermo-metamorphic carbonate formation[49]. This deep structure undergoes significant thermo-metamorphic processes, including decarbonation (calcination) that produces both CO_2 and lime[5], driven by heat from a deeper melt source[17]. Recent observations of non-magmatic CO_2 emissions during the current unrest[50], contributing 20–40% of the total fumarolic CO_2, reinforce these findings.

A similar relatively higher Vp and higher Vp/Vs anomaly was observed by Calò and Tramelli[25] at depths greater than 3 km. The authors interpreted this anomaly as a magmatic intrusion. However, the presence of intruding melt would lead to a lower Vp and a much lower Vs, both resulting in a higher Vp/Vs[18] compared to the surrounding areas.

Our study suggests that the depressurization of the gas-enriched reservoir (from 2 to 4 km depth) through the overlying fibrous microstructure of the caprock modulates seismicity. As fluids escape and the reservoir depressurizes, changes in loading conditions on the caldera's pre-existing boundary faults trigger their reactivation and lead to deeper and higher magnitude earthquakes. This high-resolution, rock physics based imaging of the caldera structure and seismicity, along with reconstruction of the dynamic evolution of the ongoing unrest, allows us to exclude the presence of magma in the first 4.5 km depth—a crucial factor for probabilistic hazard scenario[38,51,52].

By coupling the imaged structures with the evolution of seismicity, our study clearly delineates the stages of the seismicity, providing a robust foundation for understanding the mechanisms underlying the unrest at Campi Flegrei. The inferred physical processes, dominated by a "breathing" (Todesco et al. 2021) of the confined geothermal reservoir, enabled us to capture spatially regions of the caldera characterized by dynamic pore-fluid changes. This characterization, coupled with the evolution of seismicity, enables us to map how stress accumulation and release varies spatially and temporally, thus triggering seismicity. This reconstruction is crucial for assessing the physical state of the geothermal-volcanic system at Campi Flegrei and for improving the medium- and short-term multi-hazard forecasting, thereby enhancing our ability to anticipate possible future scenarios.

Time-dependent multi-hazard assessment at Campi Flegrei Caldera

Over the past 55 years, the three major bradyseismic unrest episodes (1970–1972, 1982–1984, and 2020–2024) in Campi Flegrei caldera did not culminate in eruptive activity, but they were characterized by significant ground uplift and heightened seismicity, resulting in varying degrees of structural damage and economic repercussions. During the 1982–1984 crisis, substantial damage affected buildings, roads, pipelines, and utilities, and the historic center of Pozzuoli, including the Rione Terra district, was evacuated and later underwent long-term restoration[53]. Infrastructure networks such as water and sewage lines experienced deformation, leaks, and misalignments, necessitating extensive repairs. The uplift also impacted the functionality of Pozzuoli's harbor, prompting dredging, structural modifications, and more resilient engineering designs to accommodate altered water levels as the seafloor become shallower.

Our tomographic study indicates that the observed ground deformation and the temporal, spatial, and magnitude evolution of seismicity at Campi Flegrei are largely governed by the dynamic pressure field of a subsurface, gas-rich reservoir lying between 2 and 4 km depth. Depressurization of this reservoir, driven by fluid migration, alters the stress conditions along pre-existing boundary faults within the inner caldera, ultimately triggering relatively strong earthquakes. Importantly, the absence of geophysical signatures indicative of shallow magma accumulation or transport at these depths makes significant magma involvement in the deformation process unlikely.

The spatial mapping of this extensive gas-rich reservoir at shallow depth further suggests the potential for phreatic explosions, driven by near-surface hydrothermal fluids. Such events, though not directly magma-driven, could still present substantial hazards.

Consequently, these findings highlight the need to integrate phreatic explosion scenarios into updated volcanic risk mitigation plans for the Campi Flegrei region.

The present volcanic hazard and risk strategy does not account for the impact on the community life, built environment and vital infrastructures of medium/long-term, volcano-related hazards such as earthquakes and land instabilities.

Following the approach proposed by Weir et al. [54] but aimed at managing only the volcanic eruption hazard, a statistically informed, adaptable and modular approach could be designed to develop a series of impact scenarios based on the knowledge about the secular eruptive history of the Campi Flegrei caldera and related to the occurrence of earthquake and ground uplift phenomena during the inter-eruption phases. A modular scenario development framework could consist of several modules, as, for instance, the spatial location of ground deformation and seismicity, the rate and magnitude of ground deformation and seismicity occurrence considering the possible space-time correlation, the time duration of the unrest phenomena and the frequency of occurrence of each individual hazard. Although having a lesser impact, this framework could include the geochemical hazard in the volcanic area, like gaseous and aqueous emissions in the forms of plumes, fumaroles, soil degasses and spring discharges.

The input data, empirical and numerical models allowing for the quantitative hazard assessment of each individual scenario, can be collected from the rich historical and instrumental monitoring experience at the volcano during the past 50 years. During this period, the progressively densified, multi-parametric observing system operated by INGV and DPC in the area includes now the near-real time monitoring of geochemical and geophysical parameters, that reveal earthquakes, ground deformation, gravity changes and volcanic gases composition. Data is continuously acquired, processed and timely transmitted to the Civil Protection Authorities that manage the natural hazard emergency.

Assessing and managing multi-hazard risk in Campi Flegrei caldera during inter-eruption periods requires an integrated approach where hazards, vulnerability, and exposure are combined into a single, coherent framework. This involves combining time-dependent, multi-hazard scenarios with information on critical infrastructure, population distribution, and building fragility. Analytical methods—ranging from probabilistic seismic hazard analyses and agent-based simulations—can then integrate these layers to produce quantitative risk estimates, scenario-based loss projections, and actionable risk maps. Along this direction an exemplary approach is the one illustrated in the recent work by Iervolino et al. [4]. Research integrating fault mapping, earthquake relocation, stress-drop analysis, and ground motion modeling identified the likely earthquake scenarios ranging from Mw 4.4 to 5.1. Probabilistic earthquake engineering analysis shows that code-based retrofitting would ensure that undesirable building performance only occurs at magnitudes above Mw 4.7.

Our findings spatially map three principal structures shaping the Campi Flegrei caldera. First there is a fibrous, arc-shaped horizon situated at depths of 1–2 km, which acts as a caprock seal. Below this horizon lies a gas-enriched reservoir extending from 2 to 4 km depth and displaying notably low Vp/Vs values. Dynamic rock physics experiments on cores from the reservoir, under hydrothermal conditions, provide the velocity signatures and rock deformation of fluid pressure variations and its association with changes in effective stress, thus governing the seismic activity observed in the area following the ground uplift. Finally, a thermo-metamorphic basement, marked by increasing P-wave velocities with depth and relatively high Vp/Vs values compared to the surrounding regions, dips inward toward the caldera's center.

The evolution of seismicity during unrest episodes appears closely tied to these subsurface features. Early events originate at shallower depths within the caprock and, as the reservoir degasses plausibly lowering pressure, seismicity migrates to deeper levels, producing larger-magnitude events along pre-existing faults bordering the caldera. Critically, imaging provides no evidence of magma accumulation above 4 km depth, suggesting that these episodes of ground deformation and seismicity are fluid-driven rather than the result of direct magmatic intrusion.

From a multi-hazard perspective, the dominance of fluid-related processes underscores the importance of integrating geochemical, rock physics-based seismic signatures, and ground deformation observations into hazard assessments. Deformation-related damage and phreatic explosions −rather than magmatic eruptions−pose significant threats to the densely populated region and its assets. Consequently, implementing a flexible, time-dependent multi-hazard risk management strategy becomes essential for addressing the complex and evolving risks within the Campi Flegrei caldera.

Methods

Seismic data

We used 12.681 volcano-tectonic earthquakes recorded between May 2014 and 9 November 2024 by the 21 stations of INGV network. We used P and S arrival times and magnitude estimates from the INGV earthquake catalog (https://terremoti.ov.ingv.it/gossip/flegrei). On average, each event had 7–8 P and 2–3 S arrival times and the magnitudes ranging between −1.1 and 3.5.

Inversion strategy

First, we relocate these events with NLL-SSST[30,55], which reduces the effects of velocity model errors on location, within the 1D velocity model of Vanorio et al.[18] constructed by integrating the information from wells in the area[34]. The main novelty of NLL-SSST is the use of spatially varying, source-specific station travel-time corrections (SSST) throughout a 3D volume, providing a source-position dependent correction for each station and phase type[2]. We iteratively generate SSST corrections using the catalog events and arrival data by decreasing the smoothing distances of 20, 10, 5, and 2 km, spanning from larger than the seismic pattern size to the target, sub-kilometer location precision. Within the final catalog, we selected events with rms < 0.1 s, Npha > 4 (at least 1 S phase), GAP < 220, Err<1 km. We obtained a final catalog of 10498 events that we used for the tomographic inversion. We used 75056 P-picks and 29267 S-picks. In the final catalog, 82% of events have more than 8 total phases. Moreover, 91% of events have at least 2 S picks, and 60% more than 3 S picks, reducing the cross-talk between velocity perturbation and location perturbation. Regarding the pick uncertainty, we converted in errors the weights assigned manually, following the association: weight 0 = 0.05 s, weight 1 = 0.075 s, weight 2 = 0.15 s, weight 3 = 0.35 s. Among the 75056 P-picks, the 98% has weight equal to 0, and among the 29267 S-picks, the 99% has weight 1.

This high quality catalog was used as input, together with the 1D velocity model of Vanorio et al.[18], for the 3D seismic tomography performed with a linearized method[31].

To evaluate the dependence of the final images on the choice of the initial velocity model, we performed several inversions by varying the P- and S-phase velocity models. Specifically, we randomly generated 100 P- and S-wave velocity models, allowing variability of up to 15% from the 1D models of Vanorio et al.[18] (Fig. S3). We avoided velocity inversions and constrained the Vp/Vs ratio within the expected average range for the area (1.6–1.8). We then performed a joint inversion of velocity and location parameters, starting from these 100 different velocity models with a grid parameterization of 500 m, under the same inversion conditions used in the final inversion (see details in the following lines). Our results showed that, although different initial models yielded substantially different RMS time residuals (up to 0.2 s), the data misfit of all final solutions converged to approximately the same value (~0.065 s).

Finally, to assess the stability of the final Vp/Vs model with respect to the choice of initial models, we calculated the normalized standard deviation for each Vp/Vs model node across all the final tomographic models. The resulting standard deviation values, consistently below 5% for all nodes within the resolved volumes, demonstrate the stability of our final image (see Fig. S4). For the initial P- and S-wave velocity models in our tomographic inversion, we selected the one that provided the lowest initial RMS (greed dashed line in Fig. S3).

We used a multi-scale approach for the parameterization of the tomographic model. The initial inversion runs are performed using a low-resolution, high-wavelength parameterization of the medium, which is progressively refined by increasing the density of grid points at successive runs[32]. We use a first cell size of 500 m, then reduced to 250 m with a total RMS reduction of 30% (Fig. S5). The final parameterization of the medium in the multi-scale procedure was determined using the corrected Akaike Information Criterion[56] (AICc). In assessing the possibility of reducing the parameterization, this criterion enabled us to examine the trade-off between increased model complexity (i.e., a higher number of parameters) and the corresponding reduction in data misfit. When testing a finer parameterization of 125 m, we observed an increase in the AICc value, indicating overfitting of the data. For each parameterization we optimized the inversion parameters, i.e., as damping factor, hyperparameters and smoothing factor. In detail, we used 1.5 and 1 as damping values for the 500 m and 250 m parameterizations, respectively (Fig. S6). Since the data have varying sensitivities to different parameter classes, we first eliminate the effects of parameter units and then apply weights to each class based on experimentally determined factors, named hyperparameters. These factors are derived from synthetic tests that account for our specific earthquake–station distribution, as the weighting is dependent on the configuration[31]. The chosen weights are 4 for P- and S-wave velocity parameters and 1 for location parameters, coherently with the relative number of velocity and location parameters of the inverted model. The reduction of rms in Fig. S5A and the residual distribution in Fig. S5B confirmed "a posteriori" that the adopted multiscale strategy was the most efficient to explore the multidimensional model parameter space and to catch the minimum norm model solution.

Finally, we use the final 3D tomographic models to locate the events with NLL-SSST (Fig. S1), obtaining high quality location with RMS within 0.06 s and location errors within 300 m for 70% of events (Fig. S2). The final Vp and Vp/Vs models along horizontal sections can be found in Figs. S7–S8.

Resolution assessment

For global resolution assessment, we evaluated the derivative weight sum (*DWS*) that measures the ray density in the neighborhood of every node of the tomographic grid[57]. Moreover, we validate the location and geometry of the main features of the final Vp/Vs model by performing spike tests and fixed geometry tests.

The *DWS* of the *n*th V parameters is defined as:

$$DWS(V_n) = N \sum_i \sum_j \left\{ \int_{L_{ij}} \omega_n(x) ds \right\} \quad (1)$$

where i and j are indices for event and station, ω is the linear interpolation weight that depends on coordinate position, L_{ij} is the ray path from i to j, and N is the normalization for the volume influenced by V_n. The ray-path L_{ij} is computed in the final model obtained by observation and considers the real ray-path geometry[58]. The *DWS* matrices were evaluated for each parameterization. To be conservative, we chose to

use the *DWS* of S-phase model to contour the resolved region of Vp/Vs ratio.

Since the *DWS* ranges are dependent on the single case applications, to choose the threshold value to define the resolved volume we used the results of the spike test. In detail, we select the *DWS* threshold value to bind the percentage of spike reconstruction to be greater than 80%.

In Fig. 2A, B of the main text and in Figs. S7–S10 of SM, the black or white contour delimitates the resolved area, i.e., the area for which the *DWS* values are included in the threshold value. The DWS for P and S models and for the two parameterizations (Figs. S9, S10) states that the final model is well resolved down to 4 km depth (4.5 km only for the central portion).

For the spike test analysis, a velocity perturbation of 8% was added to the Vp and Vs initial 1D models (perturbation on Vp/Vs ratio of 0.16) to simulate an increase or a decrease of the Vp/Vs ratio. This strategy is chosen to mimic the ratio trends obtained in the final models. In this view, we added noise to the synthetic travel times by mimicking the error distribution on real data, i.e., with a random Gaussian distribution with standard deviation equal to two times the sigma of real errors. The spike tests include five steps: 1) The perturbed Vp and Vs models are obtained by adding the perturbation at one grid node, 2) these models are used to compute the synthetic travel times in the source-station real configuration, 3) we added random noise to the synthetic travel-times 4) the noised times are used as input data for the tomographic inversion starting from the 1D unperturbed models and the 1D earthquake location; 5) the difference between the perturbed Vp/Vs value and the retrieved one for the selected node is evaluated. We perform the test for four slices at significant depths by repeating the described procedure for each node of the slice. We show the central portion of the investigated area (see dashed white squares in Fig. S9) at the following depths: 1) 1.5 km depth, that is the depth of caprock formation characterized by a Vp/Vs ratio increase; 2) 2.5 km depth, within the reservoir, characterized by a Vp/Vs decrease and 3) 3.5 km depth, the discontinuity between gas reservoir and basement with a Vp/Vs ratio increase. The results of the spike tests are shown in Fig. S11, the panels represent the percentage of recovery of Vp/Vs ratio, i.e., the complementary of difference between the perturbed and retrieved values at each node. The results show that the source-station configuration allowed us to reconstruct the 85% of Vp/Vs ratio anomaly, both in case of increase or decrease, within the resolved area (Fig. S11). We can discriminate between Vp/Vs ratio variation larger than 0.13.

For the fixed geometry test, we use as true model the one at 5th iteration of first parameterization of 500 m, since the main geometries can be well represented in this parameterization, and evaluated the capability to reconstruct it in the same source-station condition of the real inversion and noised data (same procedure detailed above for spike tests). The retrieved Vp/Vs ratio models coherently with the results of the spike test, contain anomalies higher than 0.13, well reconstructed in terms of location and intensity. So, we can assess that we are able to resolve the interpreted features (Fig. S12).

Rock physics experiment

The samples analyzed are volcaniclastic siltites coming from the interbedded siltites and tuffites horizon[34,37], broadly defined as tuffites and volcano-sedimentary complex by Zamora et al. [59]. The reservoir rock consists of quartz sand grains mixed with volcanic material from quaternary marine and submarine deposits. It is composed of quartz (40%), calcite (20%), clay (12%), albite (19%), orthoclase (8.1%), and zeolite Y (0.8%). This composition is consistent with findings by De Vivo et al. [35], reporting that interbedded siltites and tuffites at depths of 2–2.4 km contain illite clay, quartz, calcite, albite, and zeolite (see De Vivo et al. [35], Fig. S13).

Porosity is measured using a helium porosimeter based on Boyle's Law to determine grain and bulk densities. The reported porosity corresponds to connected porosity accessible to helium gas, with measurement uncertainties of ±1%. The error on bulk volume is evaluated as ±0.005 cm^3. The helium porosity (He-porosity) of the samples ranges from 13.5% to 19.5%, aligning with porosity data from Zamora et al. [59]. P- and S-wave velocities and their corresponding Vp/Vs ratios were measured on two samples, showing Vp values of 3192 m/s and 3128 m/s, Vs values of 1963 m/s and 1816 m/s, and Vp/Vs ratios between 1.6 and 1.7. While literature data on volcaniclastic siltites are scarce, the composition—featuring fines between quartz grains that include clays and volcanic minerals like feldspars and plagioclase—is typical of slightly tight siltites[60].

Vp and Vs are measured using the pulse transmission technique[61] under hydrostatic confining pressure conditions. These measurements are performed with a custom-built acoustic pressure vessel[62] featuring a core holder, three linear potentiometers, a pulse generator (Avtech AVR-7B-B), a switch (Hewlett Packard 4388 A), and a digital oscilloscope (Tektronix TDS 1012B; for further details on acoustic vessel system see https://srpvl.stanford.edu/Acoustic_System/). Travel time was measured after digitizing each trace with 1024 points at a time sweep of 5 ms, thus allowing a time resolution of about 5 ns or about 0.2 per cent error in velocity. Actual error in velocity measurement is estimated to be around 1 per cent due to operator error in picking first arrival.

To ensure acoustic coupling between the transducers and the sample surfaces, a high viscosity bonding medium (molasses) is applied to the flat ends of the cylindrical samples. The dry samples are then jacketed in rubber tubing to protect them from the confining pressure medium. PZT crystals mounted on steel endplates generate P- and S-waves, with frequencies of about 1 MHz for P-waves and 700 kHz for S-waves. Each endplate has a pore fluid inlet for fluid passage through the sample.

To prevent jacket leakage under conditions where pore fluid pressure (Pf) and confining pressure (Pc) were both 25 MPa, Pc was consistently maintained 0.5 MPa higher than Pf. The sample was isolated from the confining pressure system using a rubber jacket secured by conical stainless steel end caps, o-rings, and hose clamps. The end caps included inlet and outlet connections for pore pressure lines, with pressure gauges upstream and downstream ensuring equilibration of pore fluid pressure across the sample (see Fig. S14). No leakage of pore fluid into the confining medium was observed.

The temperature is controlled with a two-piece metal jacket mounted on the outside of the pressure vessel. A separate unit adjusts the temperature by switching 2000-watt heating coils on or off, allowing for rapid heating of the system.

Three linear potentiometers measure strain due to stress, which are used to estimate bulk volume and porosity changes, assuming pore closure as the main strain mechanism. The setup allows P- and S-wave measurements at various pore fluid pressures while maintaining constant confining pressure and temperature. The experiments were conducted at confining pressures of 25 MPa and 50 MPa using samples from the San Vito 1 well (depth: 2125-2134 m) corresponding to the reservoir formation (Fig. 2C in main text).

Rock saturation was achieved under pore fluid pressure in a closed vessel setup, using a core holder with upstream and downstream pressure monitoring (see Fig. S14). The dry rock was first subjected to confining pressure to measure velocity and bulk volume before fluid injection. Given the volcaniclastic siltite lithology and pore pressure magnitude, fluid pressure saturation proved more effective than vacuum saturation. Full saturation was confirmed by the equilibration of pore fluid pressure across the sample.

Data availability

The phase arrival times used in this study are available at the INGV-OV bulletin database, at the link https://terremoti.ov.ingv.it/gossip/index.html. Source data are provided with this paper. The seismic catalog, Vp and Vp/Vs velocity models, ground deformation at RITE and measures of rock physics experiment generated in this study have been deposited in the database https://zenodo.org/records/15106480[63]. The base maps used in Figures are derived from Lidar data provided by the Città Metropolitana di Napoli (https://sit.cittametropolitana.na.it/), and are licensed under the Italian Open Data License v2.0 (https://www.dati.gov.it/iodl/2.0).

Code availability

All earthquake relocations were performed with NonLinLoc[30] (http://www.alomax.net/nlloc; https://github.com/alomax/NonLinLoc). The tomographic inversion was performed with TomoTV code[31], available at https://github.com/jeanvirieux/TOMOTV_PL and has been deposited in the database at https://doi.org/10.5281/zenodo.15011755. The figures were prepared using GMT free software (https://docs.generic-mapping-tools.org/dev/install.html)[64]. Panel B in Fig. 4 and the supplementary video were constructed with *Surfer® from Golden Software, LLC (version 27*, www.goldensoftware.com), used under an educational license.

References

1. Chiodini, G. et al. Evidence of thermal-driven processes triggering the 2005–2014 unrest at Campi Flegrei caldera. *Earth Planet. Sci. Lett.* **414**, 58–67 (2015).
2. De Martino, P. et al. The ground deformation history of the Neapolitan volcanic area (Campi Flegrei caldera, Somma–Vesuvius volcano, and Ischia Island) from 20 years of continuous GPS observations (2000–2019). *Remote Sens* **13**, 2725 (2021).
3. Scotto di Uccio, F. et al. Delineation and fine-scale structure of fault zones activated during the 2014–2024 unrest at the Campi Flegrei caldera (Southern Italy) from high-precision earthquake locations. *Geophys. Res. Lett.* **51**, e2023GL107680 (2024).
4. Iervolino, I. et al. Seismic risk mitigation at Campi Flegrei in volcanic unrest. *Nat. Commun.* **15**, 10474 (2024).
5. Di Vito, M., Lirer, L., Mastrolorenzo, G. & Rolandi, G. The 1538 Monte Nuovo eruption (Campi Flegrei, Italy). *Bull. Volcanol.* **49**, 608–615 (1987).
6. Dzurisin, D. A comprehensive approach to monitoring volcano deformation as a window on the eruption cycle. *Rev. Geophys.* **41**, 1 (2003).
7. Neri, A. et al. Quantifying volcanic hazard at Campi Flegrei caldera (Italy) with uncertainty assessment: 2. Pyroclastic density current invasion maps. *J. Geophys. Res. Solid Earth* **120**, 2330–2349 (2015).
8. Stix, J. & de Moor, J. M. Understanding and forecasting phreatic eruptions driven by magmatic degassing. *Earth Planets Space* **70**, 1–19 (2018).
9. Italian Civil Protection Department. *Update of the National Emergency Plan for Campi Flegrei*. https://www.protezionecivile.gov.it/en/approfondimento/update-of-the-national-emergency-plan-for-campi-flegrei/ (2019).
10. Hill, D. P. Long Valley Caldera–Mammoth Mountain unrest: the knowns and the unknowns. *Elements* **13**, 8–9 (2017).
11. Vanorio, T. & Kanitpanyacharoen, W. Rock physics of fibrous rocks akin to Roman concrete explains uplifts at Campi Flegrei Caldera. *Science* **349**, 617–621 (2015).
12. Thurber, C. H. & Aki, K. Three-dimensional seismic imaging. *Annu. Rev. Earth Planet. Sci.* **15**, 115–144 (1987).
13. De Landro, G. et al. Decade-long monitoring of seismic velocity changes at the Irpinia fault system (southern Italy) reveals pore pressure pulsations. *Sci. Rep.* **12**, 1247 (2022).
14. Barberi, F., Hill, D. P., Innocenti, F., Luongo, G. & Treuil, M. *Bull. Volcanol* **47**, 173 (1984).
15. Aster, R. C. & Meyer, R. P. Three-dimensional velocity structure and hypocenter distribution in the Campi Flegrei Caldera, Italy. *Tectonophysics* **149**, 195–218 (1988).
16. Zollo, A. et al. Evidence for the buried rim of Campi Flegrei Caldera from 3-D active seismic imaging. *Geophys. Res. Lett.* **30**, 19 (2003).
17. Zollo, A. et al. Seismic reflections reveal a massive melt layer feeding Campi Flegrei caldera. *Geophys. Res. Lett.* **35**, 12 (2008).
18. Vanorio, T., Virieux, J., Capuano, P. & Russo, G. Three-dimensional seismic tomography from P wave and S wave microearthquake travel times and rock physics characterization of the Campi Flegrei Caldera. *J. Geophys. Res. Solid Earth* **110**, B3 (2005).
19. Chiarabba, C. & Moretti, M. An insight into the unrest phenomena at the Campi Flegrei Caldera from Vp and Vp/Vs tomography. *Terra Nova* **18**, 373–379 (2006).
20. Battaglia, J., Zollo, A., Virieux, J. & Iacono, D. Merging active and passive data sets in traveltime tomography: The case study of Campi Flegrei caldera (Southern Italy). *Geophys. Prospect.* **56**, 555–573 (2008).
21. De Siena, L. et al. Source and dynamics of a volcanic caldera unrest: Campi Flegrei, 1983–84. *Sci. Rep.* **7**, 8099 (2017).
22. Calò, M. & Tramelli, A. Anatomy of the Campi Flegrei caldera using enhanced seismic tomography models. *Sci. Rep.* **8**, 16254 (2018).
23. Amoruso, A., Crescentini, L. & Berrino, G. Simultaneous inversion of deformation and gravity changes in a horizontally layered half-space: Evidences for magma intrusion during the 1982–1984 unrest at Campi Flegrei caldera (Italy). *Earth Planet. Sci. Lett.* **272**, 181–188 (2008).
24. Giacomuzzi, G. et al. Tracking transient changes in the plumbing system at Campi Flegrei Caldera. *Earth Planet. Sci. Lett.* **637**, 118744 (2024).
25. Calò, M. & Tramelli, A. Evidences of the structures controlling the unrest in Campi Flegrei, Italy; Joint interpretation of ambient noise and local earthquake tomography. *J. Volcanol. Geotherm. Res.* **457**, 108236 (2025).
26. Astort, A. et al. Tracking the 2007–2023 magma-driven unrest at Campi Flegrei caldera (Italy). *Commun. Earth Environ.* **5**, 506 (2024).
27. Hayashi, Y. & Morita, Y. An image of a magma intrusion process inferred from precise hypocentral migrations of the earthquake swarm east of the Izu Peninsula. *Geophys. J. Int.* **153**, 159–174 (2003).
28. González, P. J. et al. Magma storage and migration associated with the 2011–2012 El Hierro eruption: implications for crustal magmatic systems at oceanic island volcanoes. *J. Geophys. Res. Solid Earth* **118**, 4361–4377 (2013).
29. Hill, D. P. Unrest in Long Valley Caldera, California, 1978–2004. *Geol. Soc. Lond. Spec. Publ.* **269**, 1–24 (2006).
30. Lomax, A. & Savvaidis, A. High-precision earthquake location using source-specific station terms and inter-event waveform similarity. *J. Geophys. Res. Solid Earth* **127**, e2021JB023190 (2022).
31. Latorre, D. et al. A new seismic tomography of Aigion area (Gulf of Corinth, Greece) from the 1991 data set. *Geophys. J. Int.* **159**, 1013–1031 (2004).
32. Bunks, C., Saleck, F. M., Zaleski, S. & Chavent, G. Multi-scale seismic waveform inversion. *Geophysics* **60**, 1457–1473 (1995).
33. De Landro, G. et al. 3D ultra-high resolution seismic imaging of shallow Solfatara crater in Campi Flegrei (Italy): New insights on deep hydrothermal fluid circulation processes. *Sci. Rep.* **7**, 3412 (2017).
34. AGIP. Modello Geotermico del Sistema Flegreo *Internal Report*, AGIP SERG-MESG, (1987).
35. de Vivo, B. et al. The Campi Flegrei (Italy) geothermal system: a fluid inclusion study of the Mofete and San Vito fields. *J. Volcanol. Geotherm. Res.* **36**, 303–326 (1989).

36. Natale, J. et al. Fault systems in the offshore sector of the Campi Flegrei caldera (Southern Italy): Implications for nested caldera structure, resurgent dome, and volcano-tectonic evolution. *J. Struct. Geol.* **163**, 104723 (2022).
37. Carella, R. & Guglielminetti, M. *Multiple reservoirs in the Mofete field, Naples, Italy (No. SGP-TR-74-5)*. *Agip SpA*, (1983).
38. Vanorio, T., Geremia, D., De Landro, G., & Guo, T. The recurrence of geophysical manifestations at the Campi Flegrei caldera. *Science Advances*, **11**, eadt2067 (2025).
39. Valadez-Gonzalez, A., Cervantes-Uc, J. M., Olayo, R. J. I. P. & Herrera-Franco, P. J. Effect of fiber surface treatment on the fiber–matrix bond strength of natural fiber reinforced composites. *Compos. Part B: Eng.* **30**, 309–320 (1999).
40. Mezeix, L., Bouvet, C., Huez, J. & Poquillon, D. Mechanical behavior of entangled fibers and entangled cross-linked fibers during compression. *J. Mater. Sci.* **44**, 3652–3661 (2009).
41. Vanorio, T., Chung, J., Siman-Tov, S. & Nur, A. Hydrothermal formation of fibrous mineral structures: The role in strength and mode of failure. *Front. Earth Sci.* **10**, 1052447 (2023).
42. Siniscalchi, A. et al. Reservoir structure and hydraulic properties of the Campi Flegrei geothermal system inferred by audio-magnetotelluric, geochemical, and seismicity study. *J. Geophys. Res. Solid Earth* **124**, 5336–5356 (2019).
43. Ellsworth, W. L. Injection-induced earthquakes. *Science* **341**, 1225942 (2013).
44. Russo, E. et al. Unraveling the complex deformation pattern at Yellowstone Plateau through seismicity and fracture analysis. *Tectonophysics* **778**, 228352 (2020).
45. Aerts, J. R. & Bilek, S. L. Characterization of earthquake clustering and swarms in Central New Mexico from 2002–2009 associated with the Socorro Magma Body. *Bull. Seismol. Soc. Am.* **115**, 115–129 (2024).
46. Tramelli, A. et al. Statistics of seismicity to investigate the Campi Flegrei caldera unrest. *Sci. Rep.* **11**, 7211 (2021).
47. Capuano, P. et al. The active portion of the Campi Flegrei caldera structure imaged by 3-D inversion of gravity data. *Geochem. Geophys. Geosyst.* **14**, 4681–4697 (2013).
48. Judenherc, S. & Zollo, A. The Bay of Naples (southern Italy): Constraints on the volcanic structures inferred from a dense seismic survey. *J. Geophys. Res.* **109**, B10312 (2004).
49. Head, D., Vanorio, T. & Clark, A. C. Elastic softening of limestone upon decarbonation with episodic CO2 release. *J. Geophys. Res. Solid Earth* **123**, 7404–7420 (2018).
50. Buono, G., Caliro, S., Pappalardo, L. & Chiodini, G. Hydrothermal calcite formation in Campi Flegrei caldera, Italy: unraveling carbon sink processes in alkaline volcanic systems. *Sci. Rep.* **14**, 16839 (2024).
51. Marzocchi, W., Sandri, L. & Selva, J. BET_EF: a probabilistic tool for long- and short-term eruption forecasting. *Bull. Volcanol.* **70**, 623–632 (2008).
52. Bell, A. F., Kilburn, C. R. & Main, I. G. Volcanic eruptions, real-time forecasting of. *Encycl. Earth Eng.* **3892**, 3906 (2016).
53. Fraiese, M., Vitiello, V. & Castelluccio, R. The effects of the Phlaegrean Bradyseism on building systems: Field research applied in Pozzuoli. *Int. J. Disaster Risk Reduct.* **113**, 104899 (2024).
54. Weir, A. M. et al. A modular framework for the development of multi-hazard, multi-phase volcanic eruption scenario suites. *J. Volcanol. Geotherm. Res.* **427**, 107557 (2022).
55. Lomax, A., Michelini, A., Curtis, A. & Meyers, R. A. Earthquake location, direct, global-search methods. *Encycl. Complex. Syst. Sci.* **5**, 2449–2473 (2009).
56. Cavanaugh, J. E. & Neath, A. A. The Akaike information criterion: Background, derivation, properties, application, interpretation, and refinements. *Wiley Interdiscip. Rev. Comput. Stat.* **11**, e1460 (2019).
57. Michelini, A. & McEvilly, T. V. Seismological studies at Parkfield. I. Simultaneous inversion for velocity structure and hypocenters using cubic B-splines parameterization. *Bull. Seismol. Soc. Am.* **81**, 524–552 (1991).
58. Rawlinson, N. & Spakman, W. On the use of sensitivity tests in seismic tomography. *Geophys. J. Int.* **205**, 1221–1243 (2016).
59. Zamora, M., Sartoris, G. & Chelini, W. Laboratory measurements of ultrasonic wave velocities in rocks from the Campi Flegrei volcanic system and their relation to other field data. *J. Geophys. Res.: Solid Earth* **99**, 13553–13561 (1994).
60. Mavko, G. M. Velocity and attenuation in partially molten rocks. *J. Geophys. Res. Solid Earth* **85**, 5173–5189 (1980).
61. Birch, F. The velocity of compressional waves in rocks to 10 kilobars: 1. *J. Geophys. Res.* **65**, 1083–1102 (1960).
62. Vanorio, T., Prasad, M., Patella, D. & Nur, A. Ultrasonic velocity measurements in volcanic rocks: correlation with microtexture. *Geophys. J. Int.* **149**, 22–36 (2002).
63. Wessel, P. et al. The Generic Mapping Tools Version 6. *Geochem. Geophys. Geosyst.* **20**, 5556–5564 (2019).
64. Wessel, P., Smith, W. H. F., Scharroo, R., Luis, J. & Wobbe, F. Generic mapping tools: improved version released. *EOS, Trans. Am. Geophys. Union* **94**, 409–410 (2013).

Acknowledgements

We thank INGV-OV (Osservatorio Vesuviano) for providing deformation data and phase picks, and Francesco Scotto di Uccio for constructing the phase file for location. The work has received financial support under the THRAM Italian Project Funded By The Call Prin 2022 Pnrr, Code P2022p37sn Project, Funded By The European Union—Next Generation Eu. This work has received financial support by the "Multi-Risk sciEnce for resilienT commUnities undeR a changiNg climate" (RETURN) project, funded by the European Union's NextGenerationEU and the Italian Ministry of University and Research (MUR) under the National Recovery and Resilience Plan (NRRP; Code PE0000005). This work has received financial support by EU through the project GOBEYOND (GA 101121135 - HORIZON-CL3-2022-DRS-01). This work has received financial support under the NSF EAR Award (#2149529) to PI T.V at Stanford University.

Author contributions

Conceptualization: A.Z., T.V., G.D.L. Methodology: J.V., A.L., G.D.L., A.Z. Software: J.V., A.L. Experiments: T.V. Formal Analysis: G.D.L., T.M. Interpretation: T.V., G.D.L. Visualization: G.D.L., T.M. Funding acquisition: A.Z., T.V., G.D.L., Supervision: T.V., A.Z., Writing – original draft: G.D.L., T.V. Writing – review & editing: G.D.L., T.V., A.Z., A.L., G.R., T.M., J.V.

Competing interests

The authors declare no competing interests.

Additional information

Supplementary information The online version contains supplementary material available at https://doi.org/10.1038/s41467-025-59821-z.

Correspondence and requests for materials should be addressed to A. Zollo.

Peer review information *Nature Communications* thanks Richard Aster, John Browning and the other anonymous reviewer(s) for their contribution to the peer review of this work. A peer review file is available.